Adaptive Finite Time Disturbance Observer-Based SPMSMs Position Sensorless Drive

Dongsong Jin, *Student Member, IEEE*, and Ling Liu, *Senior Member, IEEE*

***Abstract*—In this article, an adaptive finite time disturbance observer (FTDO)-based position sensorless drive method is proposed to improve the position and speed observation performance of surface-mounted permanent magnet synchronous motor (SPMSM). First, to observe system disturbance in a finite time, an adaptive FTDO is proposed by designing an adaptive law and combining it with a fixed time sliding surface. Due to the designed adaptive law can stably track the bound of the first-order derivative of disturbance, the adaptive FTDO does not need to know the bounds of disturbance and its first-order derivative, which will also suppress the chattering of observed disturbance. Subsequently, to compensate for the disturbance in the observed flux initially obtained by the flux observer and simultaneously observe the speed, an adaptive speed observer is designed by adopting the proposed adaptive FTDO. Besides, the finite time convergence and stability of the adaptive FTDO have been demonstrated according to the Lyapunov theory. The coefficient setting guides for adaptive FTDO are also provided. The effectiveness of the proposed adaptive FTDO-based method is verified by contrastive experiments on an SPMSM.**

***Index Terms*—Adaptive finite time disturbance observer (FTDO), position sensorless drive, speed observer, surface-mounted permanent magnet synchronous motor (SPMSM).**

Nomenclature

Let $\boldsymbol{u_s} = [u_{s\alpha}, u_{s\beta}]^{\mathrm{T}}$ and $\boldsymbol{i_s} = [i_{s\alpha}, i_{s\beta}]^{\mathrm{T}}$ denote the $\alpha\beta$-axis stator voltage vector and stator current vector, respectively, R_s denotes stator resistance, L_d and L_q represent the dq-axis stator inductances, i_d and i_q represent the dq-axis stator currents, $\boldsymbol{\psi_s} = [\psi_{s\alpha}, \psi_{s\beta}]^{\mathrm{T}}$ denotes the $\alpha\beta$-axis stator flux vector, $\boldsymbol{\psi_A} = [\psi_{r\alpha}, \psi_{r\beta}]^{\mathrm{T}} = \psi_a[\cos\theta_e, \sin\theta_e]^{\mathrm{T}}$ represents the rotor active flux vector, $\psi_a = [(L_d - L_q)i_d + \psi_f]$ designates the amplitude of $\boldsymbol{\psi_A}$, ψ_f denotes the permanent magnet flux linkage, θ_e denotes the rotor angle, ω_e represents the electrical angular speed, T_e denotes the electromagnetic torque, T_l denotes load torque, n_p denotes the number of pole pairs, J and B_ω denote the rotational inertia and frictional factor.

Received 7 April 2025; revised 7 July 2025 and 17 September 2025; accepted 20 October 2025. Date of publication 28 October 2025; date of current version 19 January 2026. This work was supported by the National Natural Science Foundation of China under Grant 51977173. Recommended for publication by Associate Editor D.-C. Lee. *(Corresponding author: Ling Liu.)*

The authors are with the State Key Laboratory of Electrical Insulation and Power Equipment, Shaanxi Key Laboratory of Smart Grid, School of Electrical Engineering, Xi'an Jiaotong University, Xi'an 710049, China (e-mail: jindongsong@stu.xjtu.edu.cn; liul@mail.xjtu.edu.cn).

Color versions of one or more figures in this article are available at https://doi.org/10.1109/TPEL.2025.3626154.

Digital Object Identifier 10.1109/TPEL.2025.3626154

I. Introduction

SURFACE-MOUNTED permanent magnet synchronous motor (SPMSM) has gained increasing popularity in various industrial fields including household appliances, electrified transportation and precision manufacturing in view of its advantages, such as strong reliability and high power density [1]. Thanks to the characteristics such as reducing the size of motor and enhancing reliability, position sensorless drive methods have been broadly studied and applied in SPMSM control [2]. At present, position sensorless drive methods are mainly divided into high frequency signal injection methods [3] for zero-low speed domain and model-based methods [4], [5] for medium-high speed domain. Although the high-frequency signal injection methods have favorable observation effect in the zero-low speed domain, they require a certain anisotropy of the motor and bring high frequency noises [6].

The model-based methods can be subdivided into the back electromotive force (EMF)-based methods and the rotor flux-based methods, with specific methods including extended state observer (ESO) [7], sliding mode observer (SMO) [8], extended Kalman filter [9], etc. However, since the amplitude of the back EMF is proportional to the speed, although the back EMF-based methods can exhibit good performance in the medium-high speed domain, it will deteriorate as the speed decreases, resulting in a narrow operational speed range for the back EMF-based methods [10], [11], [12].

Different from the back EMF, the rotor flux does not change with speed, preparing the foundation for realizing position sensorless operation of SPMSM over a wide speed range [13]. However, due to the use of integral link, disturbance including direct current (dc) bias and high order harmonics will be generated when observing the flux. To remove the generated disturbance, a frequency-adaptive observer is designed in [14], which has enhanced the accuracy of position estimation. In [15], to improve the robustness to disturbance and broaden the operating speed domain, a novel hybrid active flux observer (HAFO) based on an ESO is designed. However, these two types of observers exhibit filtering characteristics. Besides, the methods described in [14] and [15] both employ type 2 system to derive position information from the observed rotor flux. These two aspects will both limit the dynamic performance of the motor when operating over a wide speed range.

With its advantages such as strong robustness to disturbance and excellent dynamic performance, SMO has been studied and applied in the rotor flux-based methods. In [16], to enhance the robustness against model parameter mismatches, a

dual-layer adaptive sliding mode algorithm is proposed for designing a flux observer-based strategy. However, the designed adaptive algorithm is based on the equivalent control theory, which necessitates a balance between chattering suppression and dynamic performance. And the cascading use of the two observers has increased the redundancy and the computational load. To improve the dynamic performance and robustness to load, a third-order super-twisting ESO (STESO) is proposed in [17] by combining the super-twisting algorithm with ESO. Furthermore, a dual-level adaptive law for third-order STESO is designed in [18], which has extended the operating range and suppressed sliding mode ripples. However, observers such as STESO require a rough estimated rotor position, making it difficult for a single STESO to maintain robustness against model parameter mismatches. Besides, the adaptive law in [18] requires calculating a disturbance coefficient and setting the range, which poses certain difficulties for its applications. In contrast, the leakage type adaptive observers proposed in [19] do not require the range of disturbance, making it convenient for practical applications. Moreover, enlightened by the back EMF model-based SMO in [10], a flux observer that can observe the speed while filtering out the harmonics of flux is proposed in [20], which has integrated the effects of the flux observers and speed observers in the above-mentioned literatures. However, due to the adoption of constant coefficients, it is difficult to maintain the dynamic performance in a wide speed range. And the flux observer has relatively weak robustness to electrical parameter mismatches and load disturbance.

In view of the deficiencies of the flux observer in [20], adopting a sliding mode control (SMC)-based scheme to enhance it is an advisable choice. Among them, finite/fixed time SMC has been extensively studied owing to the superior convergence performance and disturbance suppression characteristics [21]. In [22], a robust nonsingular fast terminal SMC (NFTSMC) and an adaptive NFTSMC are presented. The robust NFTSMC can ensure finite time convergence, but it needs to know the bounds of disturbance. The adaptive NFTSMC does not require the bounds of disturbance, but it can only ensure the asymptotic convergence. In [23], [24], and[25], the research works on high-order fixed time SMO have been conducted. Although the integration in this kind of observer alleviates the chattering of estimated disturbance, the numerous applications of power function significantly increase the computational load, posing certain challenges for implementation in digital controllers. Besides, to observe various disturbances, a fixed time refined disturbance observer is presented in [26] based on the partially known model of disturbance. However, apart from needing to know the bounds of disturbance, it has neglected the robustness to model parameter mismatches. Moreover, a fixed time SMO is designed in [27] to estimate actuator faults and model uncertainties. In [28], an improved finite time disturbance observer (FTDO) and a novel fixed time SMO are designed, which can achieve finite time convergence and fixed time convergence, respectively. Nevertheless, the observers in [27] and [28] not only have neglected the chattering suppression in estimating disturbance, but also need to know the bounds of the first-order derivative of disturbance, which is a necessary condition to ensure finite time convergence and is difficult to be satisfied in practical systems.

Motivated by the above-mentioned discussions, an adaptive FTDO-based position sensorless drive method is proposed to enhance the position and speed observation performance of SPMSM in this article. The main contributions are summarized as follows.

1) Compared with the finite/fixed time SMO in [22], [23], [24], [25], [26], [27], and [28], by proposing an adaptive law and combining it with a fixed time sliding surface, an adaptive FTDO is presented to observe system disturbance in a finite time. Since the proposed adaptive law can stably track the bound of the first-order derivative of disturbance, this observer does not need to know the bounds of disturbance and its first-order derivative, which will also suppress the chattering of observed disturbance. Besides, only four power functions are used in this observer, making it easy to implement in practical systems.
2) Compared with the position sensorless drive methods in [12], [13], [14], [15], [16], [17], [18], and [20], by employing the proposed adaptive FTDO, an adaptive speed observer that can compensate for the disturbance in the observed flux and simultaneously observe the speed is designed, which has reduced redundancy. As each adaptive law and its fixed time sliding surface converge in a finite time, the adaptive speed observer will also converge in a finite time, which can improve the dynamic performance of the system. Moreover, owing to the robustness of SMC to disturbance and the independence of adaptive FTDO from system model, the adaptive speed observer can exhibit strong robustness to electrical parameter mismatches and load disturbance.
3) The effectiveness of the proposed adaptive FTDO-based method has been verified through contrastive experiments conducted on an SPMSM. Compared with the observers in [18] and [20], the proposed method has better dynamic performance and stronger robustness to electrical parameter mismatches and load disturbance.

II. The Existing HAFO

A. Design of HAFO

The stator voltage of SPMSM in $\alpha\beta$ axis can be written as

$$\boldsymbol{u_s} = R_s \boldsymbol{i_s} + \frac{d}{dt}\boldsymbol{\psi_s}. \tag{1}$$

Besides, $\boldsymbol{\psi_s}$ can be expressed as

$$\boldsymbol{\psi_s} = \boldsymbol{\psi_A} + L_q \boldsymbol{i_s}. \tag{2}$$

The motion equation and electromagnetic torque T_e are

$$\begin{cases} \frac{J}{n_p}\frac{d\omega_e}{dt} = T_e - T_l - \frac{B_\omega}{n_p}\omega_e \\ T_e = 1.5 n_p \psi_a i_q. \end{cases} \tag{3}$$

According to equations (1) and (2), the voltage model $\boldsymbol{\psi}_{\mathbf{A}}^{\mathbf{vm}}$ and current model $\boldsymbol{\psi}_{\mathbf{A}}^{\mathbf{cm}}$ of $\boldsymbol{\psi_A}$ can be defined as

$$\boldsymbol{\psi}_{\mathbf{A}}^{\mathbf{vm}} + L_q \boldsymbol{i_s} = \int (\boldsymbol{u_s} - R_s \boldsymbol{i_s}) dt \tag{4a}$$

$$\boldsymbol{\psi}_{\mathbf{A}}^{\mathbf{cm}} = \psi_a [\cos\theta_e, \sin\theta_e]^T. \tag{4b}$$

To initially compensate the observed error between $\boldsymbol{\psi}_{\mathbf{A}}^{\mathbf{vm}}$ and $\boldsymbol{\psi}_{\mathbf{A}}^{\mathbf{cm}}$, the observed error of the two models is fed forward to $\boldsymbol{\psi}_{\mathbf{A}}^{\mathbf{vm}}$ through a PI controller to generate a compensation quantity. Therefore, the HAFO can be expressed as

$$\begin{cases} \hat{\boldsymbol{\psi}}_{\mathbf{A0}} = \int (\boldsymbol{u_s} - R_s \boldsymbol{i_s} + \boldsymbol{Q}_{\mathbf{PI}})dt - L_q \boldsymbol{i_s} \\ \boldsymbol{Q}_{\mathbf{PI}} = (k_p + \frac{k_i}{p})(\hat{\boldsymbol{\psi}}_{\mathbf{A0}}^{\mathbf{cm}} - \hat{\boldsymbol{\psi}}_{\mathbf{A0}}) \end{cases} \tag{5}$$

where $\hat{\boldsymbol{\psi}}_{\mathbf{A0}}$ and $\hat{\boldsymbol{\psi}}_{\mathbf{A0}}^{\mathbf{cm}}$ are the observed values of the voltage model and current model, respectively, k_p and k_i are the coefficients of PI controller, p is the differential operator.

B. Disturbance of the Model

The model disturbance in HAFO mainly comes from electrical parameters mismatch. The HAFO with electrical parameters mismatch is expressed as

$$\begin{cases} \hat{\boldsymbol{\psi}}_{\mathbf{Aa}} = \int (\boldsymbol{u_s} - R_{sa} \boldsymbol{i_s} + \boldsymbol{Q}_{\mathbf{PIa}})dt - L_{qa} \boldsymbol{i_s} \\ \boldsymbol{Q}_{\mathbf{PIa}} = (k_p + \frac{k_i}{p})(\hat{\boldsymbol{\psi}}_{\mathbf{Aa}}^{\mathbf{cm}} - \hat{\boldsymbol{\psi}}_{\mathbf{Aa}}) \end{cases} \tag{6}$$

where $\hat{\boldsymbol{\psi}}_{\mathbf{Aa}}$ is the estimated rotor flux vector, R_{sa} and L_{qa} are the real-time stator resistance and inductance. Hence, $(\hat{\boldsymbol{\psi}}_{\mathbf{Aa}} - \hat{\boldsymbol{\psi}}_{\mathbf{A0}})$ can be expressed as

$$\hat{\psi}_{\mathrm{Aa}} - \hat{\psi}_{\mathrm{A0}} = (L_s - L_{sa}) i_s + \int [(R_s - R_{sa}) i_s + (Q_{\mathrm{PIa}} - Q_{\mathrm{PI}})]dt. \tag{7}$$

III. Constant Coefficient Speed Observer

The dynamic equation of $\boldsymbol{\psi}_{\mathbf{A}}$ can be expressed as

$$\begin{cases} \frac{d\psi_{r\alpha}}{dt} = -\omega_e \psi_{r\beta} + (L_d - L_q)\frac{di_d}{dt}\cos\theta_e \\ \frac{d\psi_{r\beta}}{dt} = \omega_e \psi_{r\alpha} + (L_d - L_q)\frac{di_d}{dt}\sin\theta_e. \end{cases} \tag{8}$$

To distinguish it from HAFO, the flux observer in [20] is redefined as a speed observer. Thus, the constant coefficient speed observer (CCSO) is designed as (9) [20]

$$\begin{cases} \frac{d\hat{\psi}_{r\alpha}}{dt} = -\hat{\omega}_e \hat{\psi}_{r\beta} - \lambda(\hat{\psi}_{r\alpha} - \hat{\psi}_{r\alpha 0}) \\ \frac{d\hat{\psi}_{r\beta}}{dt} = \hat{\omega}_e \hat{\psi}_{r\alpha} - \lambda(\hat{\psi}_{r\beta} - \hat{\psi}_{r\beta 0}) \\ \frac{d\hat{\omega}_e}{dt} = (\hat{\psi}_{r\alpha} - \hat{\psi}_{r\alpha 0})\hat{\psi}_{r\beta} - (\hat{\psi}_{r\beta} - \hat{\psi}_{r\beta 0})\hat{\psi}_{r\alpha} \end{cases} \tag{9}$$

where $\hat{\boldsymbol{\psi}}_{\mathbf{A}} = [\hat{\psi}_{r\alpha}, \hat{\psi}_{r\beta}]^{\mathrm{T}}$ is the estimated vector by (9), $\hat{\omega}_e$ is the estimated electrical angular speed by (9), $\hat{\psi}_{r\alpha 0}$ and $\hat{\psi}_{r\beta 0}$ correspond to $\hat{\boldsymbol{\psi}}_{\mathbf{A0}}$, and $\lambda > 0$ is the observer coefficient.

Since a stability analysis has already been conducted in [20], it will not be repeated here. Performing the Laplace transform on (9), the rotor active flux $\hat{\boldsymbol{\psi}}_{\mathbf{A}}$ can be rewritten as

$$\begin{cases} \hat{\psi}_{r\alpha} = \frac{\lambda}{s_L + \lambda}\hat{\psi}_{r\alpha 0} - \frac{\hat{\omega}_e}{s_L + \lambda}\hat{\psi}_{r\beta} \\ \hat{\psi}_{r\beta} = \frac{\lambda}{s_L + \lambda}\hat{\psi}_{r\beta 0} + \frac{\hat{\omega}_e}{s_L + \lambda}\hat{\psi}_{r\alpha} \end{cases} \tag{10}$$

where s_L is the Laplace variable. As can be seen from (10), to obtain $\hat{\boldsymbol{\psi}}_{\mathbf{A}}$, $\frac{\lambda}{s_L + \lambda}$ exhibits low-pass filtering characteristics for $\hat{\boldsymbol{\psi}}_{\mathbf{A0}}$. Although the corrections for $\hat{\psi}_{r\alpha}$ and $\hat{\psi}_{r\beta}$ that vary with $\hat{\omega}_e$ exist respectively, since λ is a constant, the CCSO must make a compromise between the dynamic performance and the steady-state performance.

IV. Proposed Adaptive FTDO for Rotor Position Information Observation

A. Proposed Adaptive FTDO

Consider a class of nonlinear systems expressed as

$$\dot{x} = f(x) + b(x)u + d \tag{11}$$

where x and u represent the system state and control input, respectively, $f(x)$ and $b(x)$ stand for the system function and control function, respectively, and d represents the system disturbance. Considering the physical system, it can be assumed that $|\dot{d}| \le \eta$ holds, where $\eta > 0$ is a constant.

To design an adaptive FTDO for (11), the state estimation error $\tilde{x}$ is first selected as $\tilde{x} = \hat{x} - x$, where $\hat{x}$ is the estimated value of x. The adaptive FTDO is designed as

$$\dot{\hat{x}} = f(\hat{x}) + b(\hat{x})u - \Sigma_{\tilde{x}} + \int \Sigma_\gamma d\tau + \gamma \tag{12}$$

where

$$\Sigma_{\tilde{x}} = k_1 \mathrm{sig}^{\alpha_1}(\tilde{x}) + l_1 \mathrm{sig}^{\beta_1}(\tilde{x}) \tag{13a}$$

$$\Sigma_\gamma = k_2 \mathrm{sig}^{\alpha_2}(\gamma) + l_2 \mathrm{sig}^{\beta_2}(\gamma) \tag{13b}$$

in (13), $\mathrm{sig}^{\alpha}(\cdot) = |\cdot|^{\alpha}\mathrm{sign}(\cdot)$, the coefficients k_j, l_j, α_j, and β_j $(j = 1, 2)$ are all positive constants, α_j and β_j satisfy $0 < \alpha_j < 1$ and $\beta_j > 1$, respectively. Besides, a sliding surface s is designed as

$$s = \dot{\tilde{x}} + k_1 \mathrm{sig}^{\alpha_1}(\tilde{x}) + l_1 \mathrm{sig}^{\beta_1}(\tilde{x}) \tag{14}$$

and the variable γ in (13) is designed as

$$\dot{\gamma} = \begin{cases} -\Sigma_\gamma - (\varepsilon + \hat{\eta})\mathrm{sign}(s), & |s| \ge \delta_0/2 \\ -\Sigma_\gamma - \frac{\varepsilon \cdot \delta_0^2}{(\delta_0 - |s|)^2}\mathrm{sign}(s), & |s| < \delta_0/2 \end{cases} \tag{15}$$

where $\hat{\eta}$ is the estimated value of η, the constants ε and δ_0 satisfy $\varepsilon, \delta_0 > 0$, the initial state of γ is labeled γ_0, and a leakage type adaptive law of $\hat{\eta}$ is designed as follows:

$$\dot{\hat{\eta}} = -\chi\hat{\eta} + |s| \tag{16}$$

where the coefficient χ is a positive constant.

Based on finite time convergence, when $\tilde{x}$ converges to zero, the estimated disturbance $\hat{d}$ can be expressed as

$$\hat{d} = \gamma + \int \Sigma_\gamma d\tau. \tag{17}$$

B. Finite Time Convergence and Stability Analysis

Enlightened by the analysis process of convergence and stability of the algorithms in [29] and [30], the results of the proposed adaptive FTDO are summarized in Theorem 1, as shown in the following, and finite time convergence and stability analysis are conducted.

Theorem 1: Consider the nonlinear system (11), in which the first-order derivative of the disturbance is bounded. When adopting the adaptive FTDO represented by (12)–(17), under the condition that the upper bound of the first-order derivative of the disturbance is unknown, the system state estimation error $\tilde{x}$ will converge to a bounded neighborhood of zero in a finite time, and at the same time, the estimated disturbance will also converge.

Proof: To analyze the conclusion as shown in (17), according to (11) and (12), differentiating $\tilde{x}$ yields

$$\dot{\tilde{x}} = \dot{\hat{x}} - \dot{x} = -\Sigma_{\tilde{x}} + \int \Sigma_\gamma d\tau + \gamma - d. \tag{18}$$

Substituting (18) into (14), s can be expressed as

$$s = \int \Sigma_\gamma d\tau + \gamma - d. \tag{19}$$

It can be known from (19) that when s converges to zero in finite time, the estimated system disturbance $\hat{d}$, as shown in (17), can be obtained.

Next, to analyze the finite time convergence and stability of s, s is discussed in different cases. When $|s| \geq \delta_0/2$, $\dot{\gamma} = -\Sigma_\gamma - (\varepsilon + \hat{\eta})\text{sign}(s)$ holds. To analyze the stability of the adaptive FTDO in this case, a Lyapunov function is first selected as $V_1 = \frac{1}{2}s^2 + \frac{1}{2}\tilde{\eta}^2$.

The derivative of V_1 is described in Appendix B. According to Lemma 1 described in Appendix A, s will converge to a bounded set s_0 in finite time t_1, where t_1 and s_0 satisfy

$$t_1 \leq T_1 = \frac{2V_1(0)^{\frac{1}{2}}}{\nu_1 \min\{\sqrt{2}\varepsilon, \frac{\chi}{\sqrt{2}}\}}, |s_0| \leq \frac{\delta_1}{(1-\nu_2)\min\{\sqrt{2}\varepsilon, \frac{\chi}{\sqrt{2}}\}} \tag{20}$$

where $V_1(0)$ is the initial state of V_1 at this stage. On the basis of (20), it can be concluded that the initial states of s and $\tilde{\eta}$ only affect the upper bound of the convergence time and do not cause the divergence of system states.

Since η is unknown, marking $\hat{\delta}_1 = (\chi + 4\chi\hat{\eta}^2)/8$. To ensure that s converges from $|s| \geq \delta_0/2$ to $|s| < \delta_0/2$, such that $\dot{\gamma} = -\Sigma_\gamma - \frac{\varepsilon\cdot\delta_0^2}{(\delta_0 - |s|)^2}\text{sign}(s)$ holds, set the δ_0 to

$$\delta_0 = \frac{2.2\hat{\delta}_1}{(1-\nu_2)\min\{\sqrt{2}\varepsilon, \frac{\chi}{\sqrt{2}}\}}. \tag{21}$$

For the convenience of stability analysis when $|s| < \delta_0/2$, the barrier function is labeled as $f_\gamma(x) = \frac{\varepsilon\delta_0^2}{(\delta_0 - |x|)^2}$, the initial time satisfying $|s(t)| \leq \frac{\delta_0}{2}$ is denoted as t_i. And assume that s_c shown in (22) exists, which satisfies $|s(t_i)| > s_c$

$$s_c = \begin{cases} \delta_0\left(1 - \sqrt{\frac{\varepsilon}{\eta}}\right), & \text{if } \varepsilon < \eta \\ 0, & \text{if } \varepsilon \geq \eta. \end{cases} \tag{22}$$

The corresponding Lyapunov function is selected as $V_2 = \frac{1}{2}s^2 + \frac{1}{2}[f_\gamma(s) - f_\gamma(0)]^2$. The derivative of V_2 and the related analysis are presented in Appendix C.

Based on the above-mentioned analysis and

Lemma 2 in Appendix A, s will converge from $s(t_i)$ to the set satisfying $|s| \leq s_c$ in finite time t_2, where t_2 satisfies the following inequality:

$$t_2 \leq T_2 = \frac{\sqrt{2}\cdot[V(s(t_i))^{\frac{1}{2}} - V(s_c)^{\frac{1}{2}}]}{(f_\gamma(s) - \eta)\cdot\min\{1, 2f_\gamma(s)\}}. \tag{23}$$

As shown in (23), $s(t_i)$ only affects the amplitude of T_2 and does not affect convergence. In summary, s in the adaptive FTDO will converge to a bounded domain in a finite time t_a, and t_a satisfies $t_a \leq T_1 + T_2$. Further, when s converges to 0 within $|s| \leq s_c$, according to (14), it can be obtained that

$$\dot{\tilde{x}} = -k_1\text{sig}^{\alpha_1}(\tilde{x}) - l_1\text{sig}^{\beta_1}(\tilde{x}). \tag{24}$$

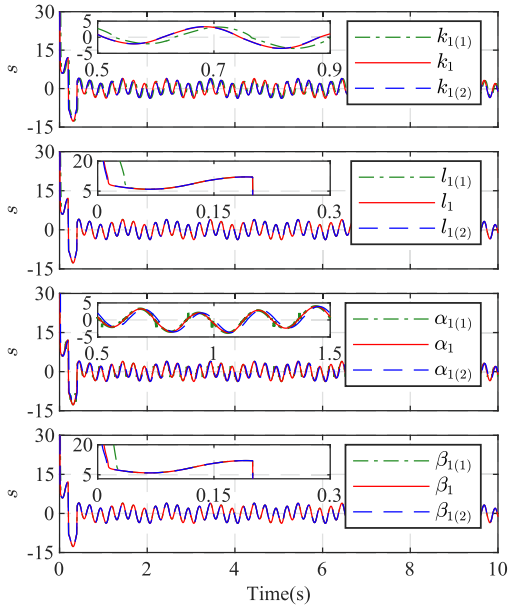

Fig. 1. Simulation results when k_1, l_1, α_1, and β_1 change, respectively.

Combining (24) and Lemma 3 in Appendix A, it can be concluded that $\tilde{x}$ will achieve fixed time convergence when $s = 0$, and the convergence time t_3 satisfies

$$t_3 \leq T_3 = \frac{1}{k_1(1-\alpha_1)} + \frac{1}{k_2(\beta_1 - 1)}. \tag{25}$$

In conclusion, when the proposed adaptive FTDO is adopted, $\tilde{x}$ will converge from any initial state to a bounded domain in a finite time t_a. When s converges to 0 within $|s| \leq s_c$, $\tilde{x}$ will converge to the origin in a finite time t_3. Meanwhile, the estimated disturbance $\hat{d}$ will also converge.

The proof of Theorem 1 is completed here.

C. Simulation Analysis

To analyze the effect of each coefficient on the adaptive FTDO, the system (26) is chosen for simulation analysis

$$\begin{cases} \dot{x}_1 = x_2 \\ \dot{x}_2 = -10x_1 - 10x_2 + u + d \end{cases} \tag{26}$$

where $d = 3\sin(8\pi t) + \cos(2\pi t)$, $u = -(\int 2|s|dt + 2) * \text{sign}(s)$, $s = 17x_1 + x_2$, the initial system states are set to $[x_1(0), x_2(0)] = [20, -20]$. Besides, in the adaptive FTDO, $k_1 = 130$, $l_1 = 100$, $\alpha_1 = 0.5$, $\beta_1 = 2$, $k_2 = 50$, $l_2 = 10$, $\alpha_2 = 0.5$, $\beta_2 = 3$, $\chi = 30$, $\varepsilon = 5$, and $\delta_0 = 2$.

Since k_1, l_1, α_1, and β_1 directly form s, for a more intuitive analysis, the simulation results of s corresponding to the changes in k_1, l_1, α_1, and β_1 from top to bottom are given in Fig. 1. Other coefficients remain unchanged, $k_{1(1)} = 60$, $k_{1(2)} = 200$. When $k_{1(1)} = 60$, s exhibits lag. Set $k_{1(2)} = 200$, s is basically the same as when $k_1 = 130$, but the computational cost increases. When only l_1 is changed, $l_{1(1)} = 10$, $l_{1(2)} = 190$. If $l_{1(2)}$ is adopted, similarly, s is basically the same as when l_1 is adopted, and the computational cost increases. While when using $l_{1(1)}$, s converges slower by about 0.02s. When only changing α_1,

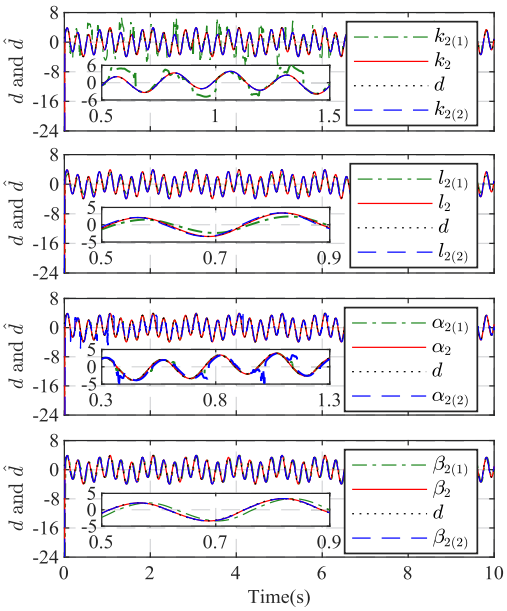

Fig. 2. Simulation results when k_2, l_2, α_2, and β_2 change, respectively.

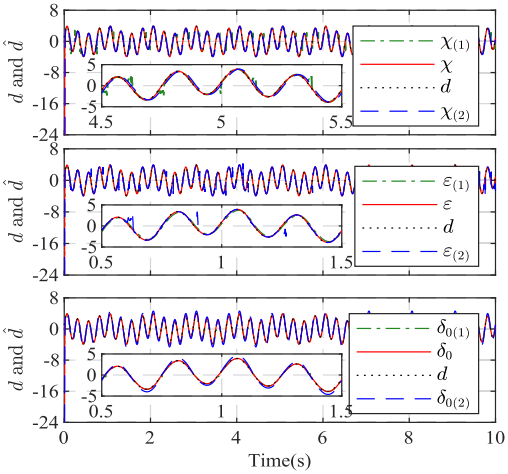

Fig. 3. Simulation results when χ, ε, and δ_0 change, respectively.

$\alpha_{1(1)} = 0.3$, $\alpha_{1(2)} = 0.7$. If using $\alpha_{1(1)}$, s is distorted near the zero-crossing point. When using $\alpha_{1(2)}$, compared with $\alpha_{1(1)}$ and α_1, s has a lag. When only β_1 is changed, $\beta_{1(1)} = 1.1$ and $\beta_{1(2)} = 2.9$. When $\beta_{1(1)}$ is adopted, the convergence of s slows down by about 0.01 s. If $\beta_{1(2)}$ is adopted, the convergence speed of s does not increase, instead, it leads to a lower simulation speed. In conclusion, as k_1, l_1, and β_1 increase and α_1 decreases, s converges. However, with the monotonic changes of these coefficients, the variation of s will become less and less obvious. Besides increasing the computational cost, it may even cause distortion of s. Conversely, as k_1, l_1, and β_1 decrease and α_1 increases, the convergence of s slows down or even diverges.

Since k_2, l_2, α_2, β_2, χ, ε, and δ_0 directly affect $\hat{d}$, Fig. 2 shows the simulation results of $\hat{d}$ with changes in k_2, l_2, α_2, and β_2 in sequence, and Fig. 3 shows the simulation results of $\hat{d}$ with changes in χ, ε, and δ_0 in sequence. As shown in Fig. 2, when only k_2 is changed, $k_{2(1)} = 5$, $k_{2(2)} = 100$. When k_2 is set to $k_{2(1)}$, $\hat{d}$ is

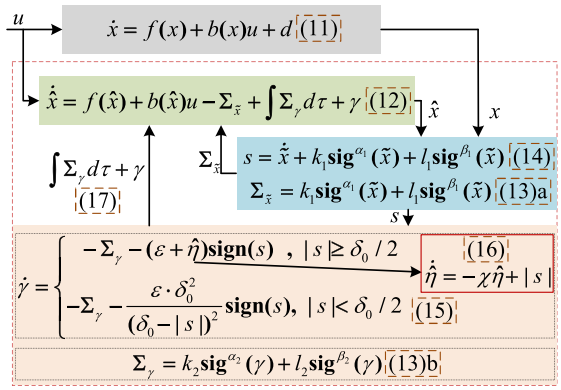

Fig. 4. Implementation architecture of the proposed adaptive FTDO.

difficult to converge to s. If k_2 is set to $k_{2(2)}$, $\hat{d}$ remains basically unchanged, but the computational load will increase. When only l_2 is changed, $l_{2(1)} = 0.5$, $l_{2(2)} = 100$. If l_2 is set to $l_{2(1)}$, $\hat{d}$ not only has hysteresis, but also amplitude attenuation. When l_2 is set to $l_{2(2)}$, similar to $k_{2(2)}$, the simulation speed will be reduced. Next, when analyzing α_2, $\alpha_{2(1)} = 0.3$, $\alpha_{2(2)} = 0.7$. If α_2 is set to $\alpha_{2(1)}$, $\hat{d}$ diverges near the zero-crossing point. When α_2 is set to $\alpha_{2(2)}$, $\hat{d}$ not only diverges near the zero-crossing point, but also has a certain delay. When analyzing β_2, $\beta_{2(1)} = 1.5$, $\beta_{2(2)} = 4.5$. If β_2 is set to $\beta_{2(1)}$, $\hat{d}$ generates phase delay. When β_2 is set to $\beta_{2(2)}$, $\hat{d}$ changes little, but the computational cost will increase. According to the above-mentioned analysis and (13), the changing trends of k_2, l_2, α_2, and β_2 have the same effect on $\hat{d}$ as k_1, l_1, α_1, and β_1 have on s.

The analysis of the remaining coefficients is shown in Fig. 3. When analyzing the impact of χ, $\chi_{(1)} = 5$, $\chi_{(2)} = 55$. After setting χ to $\chi_{(1)}$, $\hat{d}$ diverges near the zero-crossing point. Set χ to $\chi_{(2)}$, phase delay occurs in $\hat{d}$. Combined with (16) for analysis, χ also needs to be gradually adjusted and balanced between the convergence rate and the observed waveform. When analyzing ε, $\varepsilon_{(1)} = 0.5$, $\varepsilon_{(2)} = 50$. If ε is set to $\varepsilon_{(1)}$, it can be seen that not only phase delay but also amplitude attenuation occurs in $\hat{d}$. After setting ε to $\varepsilon_{(2)}$, $\hat{d}$ diverges near the zero-crossing point. It can be seen that a smaller ε does not cause distortion of $\hat{d}$, so ε can be gradually increased from a smaller initial value according to the observation effect. When analyzing δ_0, $\delta_{0(1)} = 0.5$, $\delta_{0(2)} = 10$. Setting δ_0 to $\delta_{0(1)}$, $\hat{d}$ has a divergence phenomenon near the zero-crossing point, but it can converge to d quickly. When $\delta_{0(2)}$ is adopted, it can be seen that the amplitude of $\hat{d}$ is greater than d at this time, which indicates that the estimated value is biased. Thus, to ensure the accuracy of $\hat{d}$, the basic range of s should be observed first, and δ_0 should be set within this range.

D. Coefficient Setting Guides

To make the application of the proposed adaptive FTDO more convenient and intuitive, the architecture of the observer is presented in Fig. 4, and the coefficient setting guides of the observer are shown as follows.

1) The coefficients in $\Sigma_{\tilde{x}}$ determines the convergence time of s. Based on the simulation results shown in Fig. 1 and the corresponding analysis, the coefficients in $\Sigma_{\tilde{x}}$ can be initially set to $k_1 = 100, l_1 = 100, \alpha_1 = 0.5$, and $\beta_1 = 2$, which will ensure the convergence of s.
2) According to the simulation results shown in Fig. 2 and the corresponding analysis, the coefficients in Σ_γ will directly affect $\hat{d}$. To balance the observation effect and computational complexity, the coefficients in Σ_γ are initially set to $k_2 = 20, l_2 = 5, \alpha_2 = 0.5$, and $\beta_2 = 2$.
3) In the other coefficients, as shown in Fig. 3, an initial value of χ can be given first, and then χ can be adjusted based on the observation effect of $\hat{d}$. ε should not only ensure the stability of the algorithm, but also avoid severe chattering of $\hat{d}$. In addition, according to the discussion of Fig. 3, δ_0 can be firstly set to a smaller value after observing the amplitude of s in step 1, and then adjusted appropriately. Thus, these coefficients are initially set to $\chi = 20, \varepsilon = 2$, and $\delta_0 = 2$.

After initializing the coefficients through the above-mentioned steps, each coefficient should be fine-tuned according to the observation effect of the system states and the role of the coefficients.

E. Adaptive Speed Observer Based on the Adaptive FTDO

To achieve better comprehensive performance of the system, an adaptive speed observer is designed based on the proposed adaptive FTDO and SPMSM model, as shown in

$$\frac{d\hat{\psi}_{r\alpha}}{dt} = -\hat{\omega}_e\hat{\psi}_{r\beta} - \Sigma_{\tilde{\psi}_{r\alpha}} + \int \Sigma_{\gamma_\alpha} d\tau + \gamma_\alpha \tag{27a}$$

$$\frac{d\hat{\psi}_{r\beta}}{dt} = \hat{\omega}_e\hat{\psi}_{r\alpha} - \Sigma_{\tilde{\psi}_{r\beta}} + \int \Sigma_{\gamma_\beta} d\tau + \gamma_\beta \tag{27b}$$

$$\frac{d\hat{\omega}_e}{dt} = \frac{1.5n_p^2\psi_a}{J} i_q^* - \Sigma_{\tilde{\omega}_e} + \int \Sigma_{\gamma_\omega} d\tau + \gamma_\omega \tag{27c}$$

where $\tilde{\psi}_{r\alpha} = \hat{\psi}_{r\alpha} - \hat{\psi}_{r\alpha 0}$, $\tilde{\psi}_{r\beta} = \hat{\psi}_{r\beta} - \hat{\psi}_{r\beta 0}$, $\tilde{\omega}_e = \hat{\omega}_e - \hat{\omega}_{e0}$, and $\hat{\theta}_{e0} = \arctan(\hat{\psi}_{r\beta 0}/\hat{\psi}_{r\alpha 0})$, $\hat{\omega}_{e0} = d\hat{\theta}_{e0}/dt$. Besides

$$\begin{cases} \Sigma_{\tilde{y}} = k_{y1}\mathrm{sig}^{\alpha_{y1}}(\tilde{y}) + l_{y1}\mathrm{sig}^{\beta_{y1}}(\tilde{y}) \\ \Sigma_{\gamma_z} = k_{z2}\mathrm{sig}^{\alpha_{z2}}(\gamma_z) + l_{z2}\mathrm{sig}^{\beta_{z2}}(\gamma_z) \end{cases} \tag{28}$$

where $y = \psi_{r\alpha}, \psi_{r\beta}, \omega_e$, $z = \alpha, \beta, \omega$. The corresponding sliding surface s_y can be expressed as

$$s_y = \dot{\tilde{y}} + k_{y1}\mathrm{sig}^{\alpha_{y1}}(\tilde{y}) + l_{y1}\mathrm{sig}^{\beta_{y1}}(\tilde{y}). \tag{29}$$

The corresponding variable γ_z in (28) is rewritten as

$$\dot{\gamma}_z = \begin{cases} -\Sigma_{\gamma_z} - (\varepsilon_z + \hat{\eta}_z)\mathrm{sign}(s_y), & |s_y| \geq \delta_{y0}/2 \\ -\Sigma_{\gamma_z} - \frac{\varepsilon_z \cdot \delta_{y0}^2}{(\delta_{y0} - |s_y|)^2}\mathrm{sign}(s_y), & |s_y| < \delta_{y0}/2 \end{cases} \tag{30}$$

where

$$\dot{\hat{\eta}}_z = -\chi_z\hat{\eta}_z + |s_y|. \tag{31}$$

In addition, $\hat{\theta}_e$ can be obtained from the rotor flux estimated by the adaptive speed observer, as expressed in

$$\hat{\theta}_e = \arctan(\frac{\hat{\psi}_{r\beta}}{\hat{\psi}_{r\alpha}}). \tag{32}$$

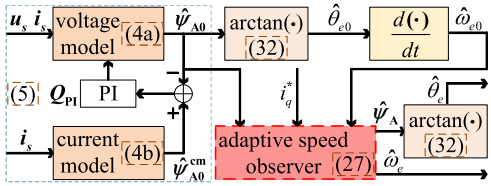

Fig. 5. Implementation architecture of the HAFO and the proposed adaptive speed observer.

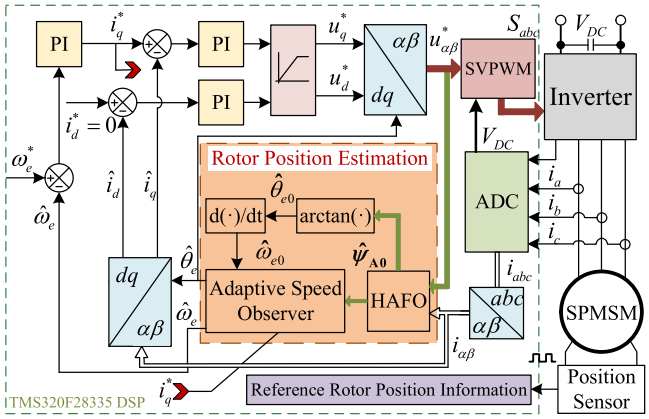

Fig. 6. Whole framework of SPMSM position sensorless control system.

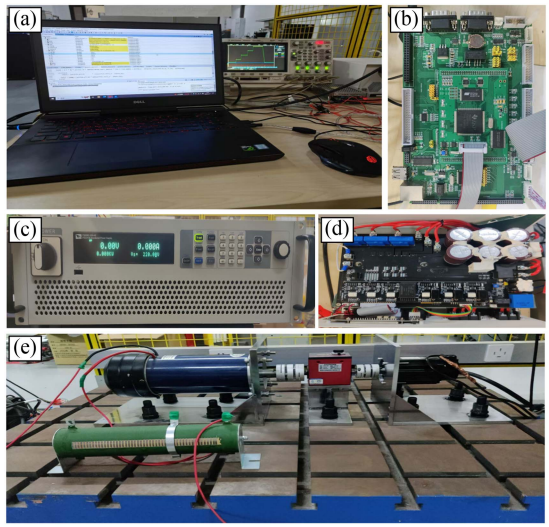

Fig. 7. Experimental setup of SPMSM drives. (a) Debugging computer and oscilloscope. (b) DSP controller. (c) DC power supply. (d) Converter. (e) Motor towing platform.

The implementation architecture for observing rotor position information based on the HAFO and the proposed adaptive speed observer is shown in Fig. 5.

V. Experimental Verification

The whole framework of the SPMSM position sensorless control system is designed as Fig. 6. And a motor towing platform using a 750 W SPMSM is built as Fig. 7 to evaluate the performance of the proposed method. In the test bench, DSP TMS320F28335 is employed as the main control chip, and the relevant parameters of the tested SPMSM are listed in

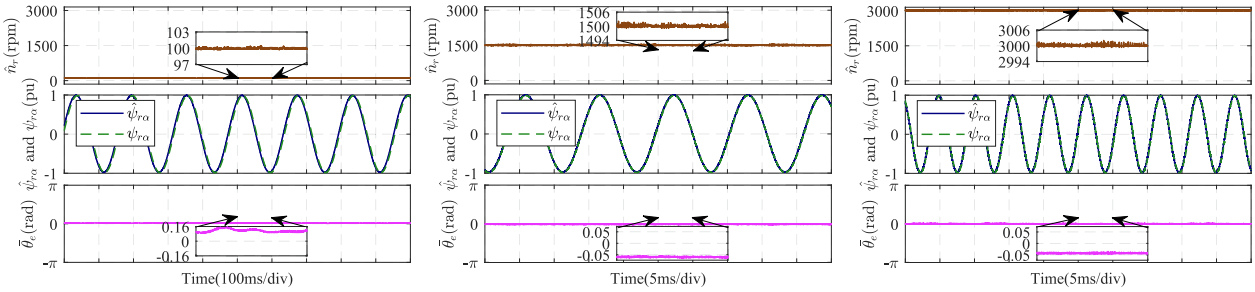

Fig. 8. Experimental results of $\hat{n}_r$, $\hat{\psi}_{r\alpha}$, and $\psi_{r\alpha}$, and $\bar{\theta}_e$ at (a) 100, (b) 1500, and (c) 3000 rpm using the proposed adaptive FTDO-based method.

TABLE I
RELEVANT PARAMETERS OF THE CONTROLLED SPMSM

Parameter	Value	Parameter	Value
Rated voltage U_n	220 V	PM flux linkage ψ_f	0.0936 Wb
Stator resistance R_s	1.38 Ω	Rated torque T_{eN}	2.39 N·m
Stator inductance L_s	3.21 mH	Rated speed n_N	3000 r/min

TABLE II
COEFFICIENTS USED IN THE ADAPTIVE FTDO-BASED SPEED OBSERVER

Equation	Coefficients
eq. (27a)	$k_{\psi_{r\alpha}1}=125$, $l_{\psi_{r\alpha}1}=125$, $\alpha_{\psi_{r\alpha}1}=0.5$, $\beta_{\psi_{r\alpha}1}=2$, $k_{\alpha 2}=3$, $l_{\alpha 2}=0.3$, $\alpha_{\alpha 2}=0.5$, $\beta_{\alpha 2}=2$, $\varepsilon_\alpha=10$, $\chi_\alpha=12$
eq. (27b)	$k_{\psi_{r\beta}1}=125$, $l_{\psi_{r\beta}1}=125$, $\alpha_{\psi_{r\beta}1}=0.5$, $\beta_{\psi_{r\beta}1}=2$, $k_{\beta 2}=3$, $l_{\beta 2}=0.3$, $\alpha_{\beta 2}=0.5$, $\beta_{\beta 2}=2$, $\varepsilon_\beta=10$, $\chi_\beta=12$
eq. (27c)	$k_{\omega_e}1=20$, $l_{\omega_e}1=10$, $\alpha_{\omega_e}1=0.5$, $\beta_{\omega_e}1=1.5$, $k_{\omega 2}=0.1$, $l_{\omega 2}=0.1$, $\alpha_{\omega 2}=0.5$, $\beta_{\omega 2}=2$, $\varepsilon_\omega=10$, $\chi_\omega=12$

Table I. In the experiment, the PWM carrier frequency, sampling frequency and switching frequency of the converter are all set to 10 kHz. Besides, to obtain reference rotor position information, an incremental encoder is installed on the SPMSM. To generate the load torque, a dc motor connected with a sliding rheostat is linked with the SPMSM. And the I-F control method is adopted to start the motor. In this section, comparative experiments are carried out among HAFO + CCSO in [20], HAFO + adaptive STESO in [18], and HAFO + the adaptive FTDO-based speed observer. In the CCSO, $\lambda = 200$. In the adaptive STESO in [18], $\alpha_1 = 50$, $\lambda = 20$, $\chi = 0.8$. In the adaptive FTDO-based speed observer, the coefficients of each equation in (27a), (27b), and (27c) are all reflected in (28), (30), and (31). The estimated variables of different equations in (27a), (27b), and (27c) are distinguished by $y = \psi_{r\alpha}, \psi_{r\beta}, \omega_e$, while the estimated disturbances are distinguished by $z = \alpha, \beta, \omega$. The coefficients of each equation are listed in Table II. In the experimental results, $\hat{n}_r$, n_r, and n_r^*, respectively, denote the estimated speed, the measured speed and the reference speed, $\bar{n}_r = n_r - \hat{n}_r$ represents the speed estimation error, $\hat{\psi}_{r\alpha}$ and $\psi_{r\alpha}$, respectively, denote the estimated rotor flux and the calculated rotor flux of α-axis, $\bar{\theta}_e$ indicates the position estimation error.

A. Steady-State Performance Analysis

The steady-state experimental results of $\hat{n}_r$, $\hat{\psi}_{r\alpha}$, and $\psi_{r\alpha}$, and $\bar{\theta}_e$ at 100, 1500, and 3000 rpm using the proposed adaptive FTDO-based method are shown in Fig. 8. As shown in Fig. 8(a), when the motor runs at 100 rpm, $\hat{n}_r$ does not exhibit significant chattering within the range of 3 rpm. Besides, although $\bar{\theta}_e$ can reach a maximum of 0.16 rad, $\bar{\theta}_e$ remains stable at about 0.1 rad, and $\hat{\psi}_{r\alpha}$ can track $\psi_{r\alpha}$ well. As the speed increases, as shown in Fig. 8(b) and (c), when the motor runs at 1500 or 3000 rpm, neither $\hat{n}_r$ shows significant chattering within the range of 6 rpm, and the absolute value of $\bar{\theta}_e$ decreases, fluctuating around 0.05 rad. The finite time convergence of the adaptive speed observer achieves the convergence of rotor flux and speed in a finite time, ensuring favorable steady-state performance.

B. Dynamic Performance Analysis

The dynamic performance experimental results under various operating conditions using the CCSO in [20], the adaptive STESO in [18], and the proposed adaptive FTDO-based method are shown in Figs. 9 to 13.

Fig. 9 shows the results of continuous slope reversal test between 1500 and –1500 rpm using different observers. As shown in Fig. 9(a), when adopting the CCSO, $\bar{n}_r$ changes continuously during the testing process, with a maximum of over 100 rpm. And the maximum $\bar{\theta}_e$ will exceed $\pi/2$. In Fig. 9(b), when adopting the adaptive STESO, during the entire process, only when n_r is close to zero does $\bar{n}_r$ increase. And the maximum $\bar{n}_r$ can even reach up to 200 rpm, corresponding to a sudden increase in $\bar{\theta}_e$ to nearly $\pi/2$. Besides, $\bar{\theta}_e$ is about 0.05 rad when the motor runs at 1500 rpm. And when the speed is increased to 1500 rpm or decreased from 1500 rpm, $\bar{\theta}_e$ changes slightly, with a maximum of approximately 0.1 rad. In contrast, in Fig. 9(c), when the adaptive FTDO-based method is adopted, $\bar{n}_r$ fluctuates around zero at a speed scale of 50 rpm, proving that $\hat{n}_r$ can track n_r well. Although $\bar{\theta}_e$ still increases at the zero crossing point, $\bar{\theta}_e$ significantly decreases, with a maximum value of approximately 0.23 rad. When the motor runs at 1500 rpm, $\bar{\theta}_e$ also fluctuates around 0.05 rad. Only when the speed is increased to 1500 rpm or decreased from 1500 rpm, does the $\bar{\theta}_e$ exceed 0.1 rad.

Fig. 10 shows the results of continuous step reversal test between 200 and –200 rpm. When the CCSO is used, as shown in Fig. 10(a), significant $\bar{n}_r$ and $\bar{\theta}_e$ exist during the reversing

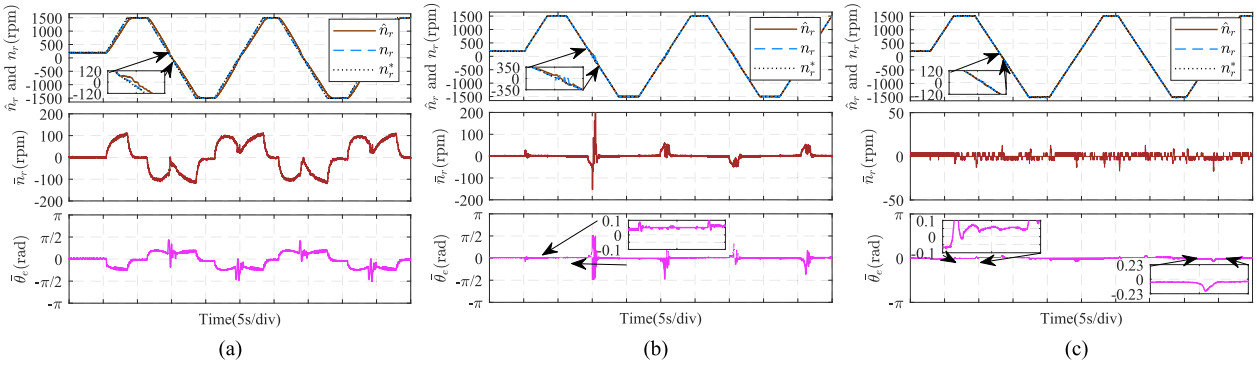

Fig. 9. Experimental results of $\hat{n}_r$, n_r and n_r^*, $\bar{n}_r$ and $\bar{\theta}_e$ in continuous slope reversal test between 1500 and –1500 rpm using different observers. (a) CCSO in [20]. (b) Adaptive STESO in [18]. (c) Proposed adaptive FTDO-based method.

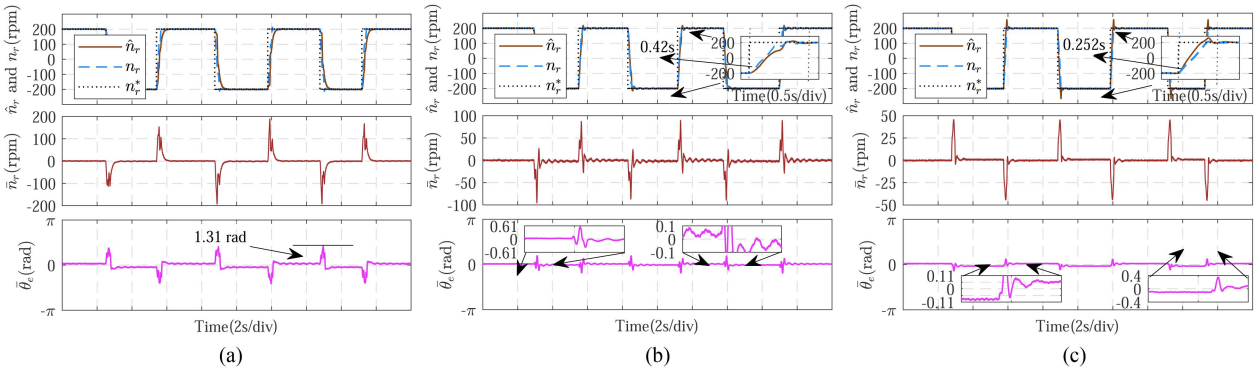

Fig. 10. Experimental results of $\hat{n}_r$, n_r and n_r^*, $\bar{n}_r$ and $\bar{\theta}_e$ in continuous step reversal test between 200 and –200 rpm using different observers. (a) CCSO in [20]. (b) Adaptive STESO in [18]. (c) Proposed adaptive FTDO-based method.

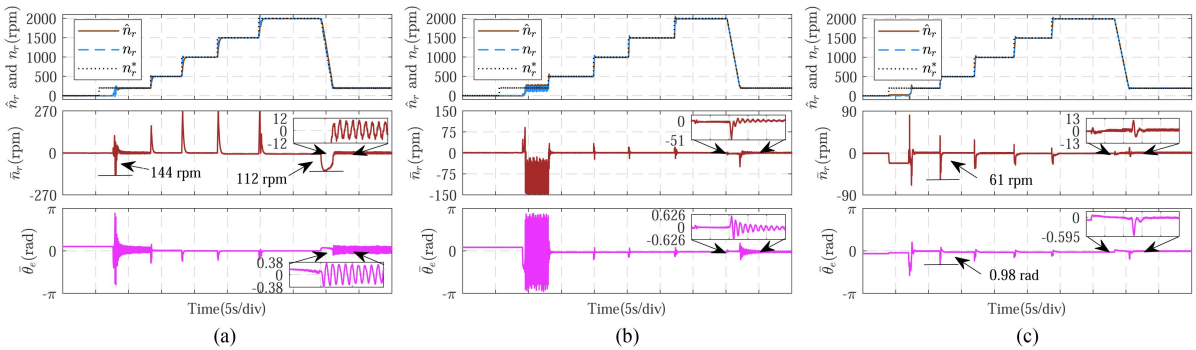

Fig. 11. Experimental results of $\hat{n}_r$, n_r and n_r^*, $\bar{n}_r$ and $\bar{\theta}_e$ in comprehensive variable speed test using different observers. (a) CCSO in [20]. (b) Adaptive STESO in [18]. (c) Proposed adaptive FTDO-based method.

process, which can reach about 200 rpm and 1.31 rad, respectively. In the waveform diagrams of $\bar{\theta}_e$ in Fig. 10(b) and (c), the positions with the maximum amplitude of $\bar{\theta}_e$ during the dynamic process and the steady state process, respectively, are selected for local amplification. In Fig. 10(b), when adopting the adaptive STESO, the maximum values of $\bar{n}_r$ and $\bar{\theta}_e$ decrease, at around 90 rpm and 0.61 rad, respectively. In addition, $\bar{\theta}_e$ fluctuates within 0.1 rad during the steady state process. When using the proposed method, as shown in Fig. 10(c), $\bar{n}_r$ and $\bar{\theta}_e$ are greatly reduced, in which $\bar{n}_r$ is within 50 rpm and $\bar{\theta}_e$ is within 0.4 rad. During the steady state process, the maximum amplitude of $\bar{\theta}_e$ is close to 0.11 rad. Based on the analysis of $\bar{\theta}_e$ in Figs. 9 and 10, due to the coupling of speed and flux in the adaptive FTDO-based method, a sudden increase in $\bar{\theta}_e$ may occur during the dynamic process, even exceeding that in the adaptive STESO. However, with the finite time convergence of adaptive FTDO, $\bar{\theta}_e$ will converge rapidly. In the steady state process, $\bar{\theta}_e$ will be basically equal to that in the adaptive STESO. Moreover, comparing Fig. 10(b) and (c), it can be seen that the time taken for the speed to increase from –200 to 200 rpm in Fig. 10(c) is about 0.252 s, which is about 0.168 s faster than that in Fig. 10(b). The proposed method exhibits better

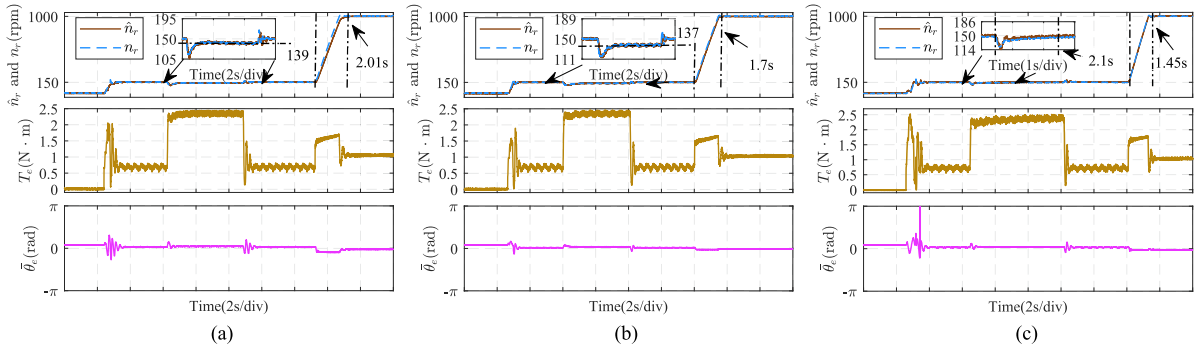

Fig. 12. Experimental results of $\hat{n}_r$ and n_r, T_e and $\bar{\theta}_e$ in step load and acceleration test using different observers. (a) CCSO in [20]. (b) Adaptive STESO in [18]. (c) Proposed adaptive FTDO-based method.

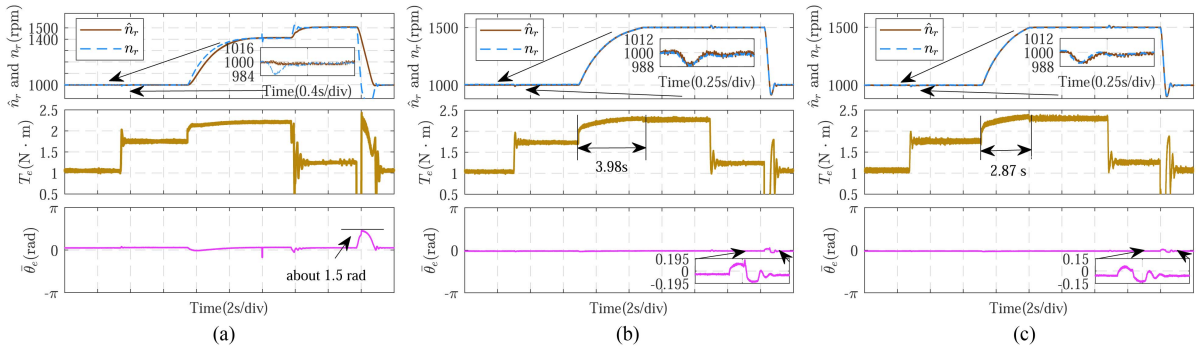

Fig. 13. Experimental results of $\hat{n}_r$ and n_r, T_e and $\bar{\theta}_e$ in simultaneous acceleration and loading test using different observers. (a) CCSO in [20]. (b) Adaptive STESO in [18]. (c) Proposed adaptive FTDO-based method.

dynamic performance. However, for the sake of fair comparison, the parameters of the speed PI controller and current PI controller remain unchanged when using different observers. This results in smaller overshoot for the other two observers, while the speed has a certain overshoot in the proposed method. To reduce the overshoot, the PI parameters of the controllers can be adjusted to appropriately increase the speed regulation time of the proposed method.

Experimental results of comprehensive variable speed test adopting the three types of speed observers are shown in Fig. 11. In this type of test, the motor is lightly loaded with a load torque of about 0.32 N · m. After a reference speed is given, it waits to start. During startup, different types of methods are used to directly accelerate the motor from static to 200 rpm. Afterward, the speed change in the acceleration process is 200–500–1000–1500–2000 rpm, and then the reference speed ramp decelerates to 200 rpm. In this test, the dc bus voltage is increased to 220 V to achieve wider speed range operation, which results in an increase in voltage harmonics in the low speed range, thereby reducing the signal-to-noise ratio (SNR) and increasing the initial value of $\bar{\theta}_e$. When the CCSO is used, as presented in Fig. 11(a), as the dc bus voltage increases, the operating performance in the low-speed domain deteriorates. At 200 rpm, not only does $\bar{n}_r$ fluctuate with an amplitude of 12 rpm, but also $\bar{\theta}_e$ changes with an amplitude of about 0.38 rad. Besides, in the step acceleration process, the maximum $\bar{n}_r$ is close to 270 rpm, and the peak value of $\bar{n}_r$ during deceleration is about 112 rpm. In Fig. 11(b), when using the adaptive STESO, since the adaptive STESO requires a smaller $\bar{\theta}_e$, it is difficult for the motor to operate stably when directly accelerating the motor to 200 rpm. Although the motor could not operate stably when directly accelerated to 200 rpm, the speed tracking is good throughout the process, with the maximum values of $\bar{n}_r$ and $\bar{\theta}_e$ being about 51 rpm and 0.626 rad, respectively. Fig. 11(c) presents the result obtained using the adaptive FTDO-based method. After the reference speed is given and while waiting for startup, a $\bar{n}_r$ of about 20 rpm can be observed. This is because the motor has an unknown initial position, which leads to an observation error of flux in the adaptive speed observer. The coupled relationship between speed observation and flux observation, as well as the finite time convergence of the adaptive FTDO, result in the $\bar{n}_r$. Except during startup, when the speed increases from 200 to 500 rpm, the amplitudes of $\bar{n}_r$ and $\bar{\theta}_e$ are the highest, approaching 61 rpm and 0.98 rad, respectively. After each speed change, both $\bar{n}_r$ and $\bar{\theta}_e$ converge quickly. Besides, during the deceleration process, n_r can be well tracked, and the maximum $\bar{n}_r$ is about 13 rpm.

The comparative tests and analyses in Figs. 9–11 confirm the excellent dynamic performance of the proposed method. Compared with the CCSO in [20], the finite time convergence of the proposed adaptive FTDO provides a guarantee for the convergence of errors in dynamic processes. Compared with the adaptive STESO in [18], the proposed method not only has finite time convergence, but also couples the observation of rotor flux

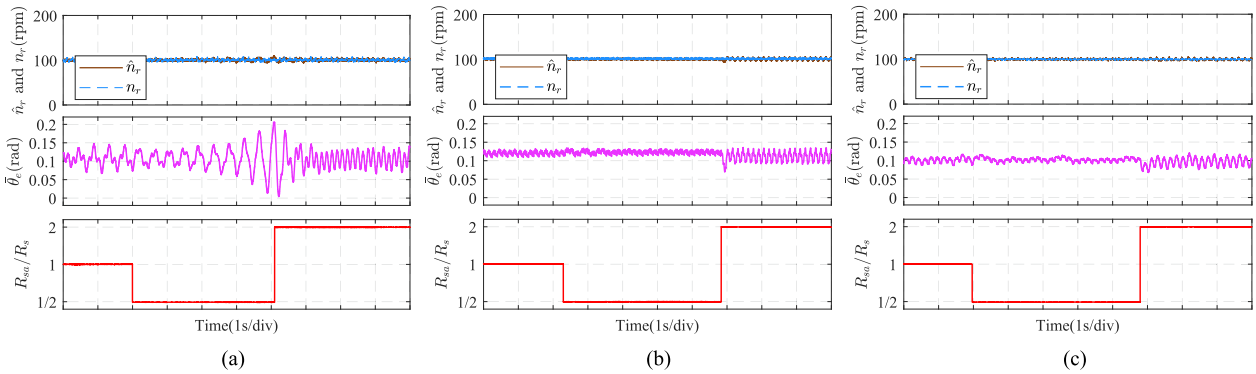

(a) (b) (c)

Fig. 14. Experimental results of $\hat{n}_r$, n_r, and $\bar{\theta}_e$ when R_s changes using different observers at 100 rpm. (a) CCSO in [20]. (b) Adaptive STESO in [18]. (c) Proposed adaptive FTDO-based method.

with speed, which has improved the SNR of the observed signals in the low speed domain.

Fig. 12 presents the test results of first step loading and unloading, and then step acceleration. In this test, the motor is directly started to 150 rpm using the position sensorless drive methods. At this point, the motor carries a load of about 0.7 N · m. Then, a step load of 1.65 N · m is added. After stable operation, the step load of 1.65 N · m is removed. Afterward, the motor is accelerated to 1000 rpm. In Fig. 12(a) and (b), when adding a step load of 1.65 N · m, n_r decreases by about 45 and 39 rpm, respectively. After stabilizing, n_r is difficult to recover to 150 rpm, and n_r in Fig. 12(a) is around 139 rpm, n_r in Fig. 12(b) is around 137 rpm. This is because although both the CCSO and the adaptive STESO have estimated and compensated for disturbance in the motion equation, the CCSO estimates disturbance based on the flux observation errors and needs to adjust the constant coefficient. The adaptive STESO needs to adjust the disturbance coefficient. The disturbance compensation effects are all limited. When increasing n_r from 150 to 1000 rpm, it takes about 2.01 s in Fig. 12(a) and about 1.7 s in Fig. 12(b). Due to the large moment of inertia and friction of the dc motor used, the load torque increases from about 0.7 N · m to about 1.05 N · m as the speed increases. In the experiment corresponding to Fig. 12(b), because of the narrowed operating speed range, the dc bus voltage is reduced to 150 V. And the SNR increases when the motor operates at low speed range, so the motor can be directly and stably accelerated to 150 rpm. In contrast, in Fig. 12(c), when the adaptive FTDO-based method is used, although n_r decreases by about 36 rpm when a load of 1.65 N · m is applied, it returns to 150 rpm after about 2.1 s, achieving a good speed tracking effect. And the acceleration process takes about 1.45 s, faster than the other two methods.

In the simultaneous acceleration and loading test, as shown in Fig. 13, the motor first runs stably at 1000 rpm with a load of 1.05 N · m, and then a step load of 0.7 N · m is added. After stable operation, n_r is increased from 1000 to 1500 rpm. In Fig. 13(a), with the CCSO, it is difficult for the motor to reach 1500 rpm during the acceleration process. After unloading the load of about 0.95 N · m, n_r rises to 1500 rpm. Besides, when n_r drops from 1500 to 1000 rpm, not only n_r and T_e fluctuate greatly, but also $\bar{\theta}_e$ produces a peak of about 1.5 rad. In Fig. 13(b) and (c), when the adaptive STESO and the adaptive FTDO-based method are respectively adopted, n_r can be increased from 1000 to 1500 rpm, while T_e is increased from 1.75 N · m to about 2.3 N · m. However, in Fig. 13(c), it takes about 2.87 s for n_r to rise from 1000 to 1500 rpm, while in Fig. 13(b), the time is about 3.98 s. Besides, when n_r is decreased from 1500 to 1000 rpm, the peaks of $\bar{\theta}_e$ in Fig. 13(b) and (c) are 0.195 and 0.15 rad, respectively.

According to the analysis of Figs. 12 and 13, compared with the CCSO in [20] and the adaptive STESO in [18], the adaptive FTDO-based method has stronger load capacity and shorter acceleration time.

C. Electrical Parameters Sensitivity Analysis

Experimental results of different electrical parameter mismatches using the three types of methods operating at 100 rpm with a load of 0.32 N · m are shown in Figs. 14–16.

In the sensitivity analysis of R_s, as shown in Fig. 14(a), if the CCSO is adopted, after $R_{sa}/R_s = 1/2$ is set, $\bar{\theta}_e$ begins to diverge, with peaks even exceeding 0.2 rad. When changed to $R_{sa}/R_s = 2$, $\bar{\theta}_e$ converges with a peak value of about 0.14 rad. In comparison, in Fig. 14(b) and (c), when adopting the adaptive STESO or the adaptive FTDO-based method, after $R_{sa}/R_s = 1/2$ is set, although $\bar{\theta}_e$ fluctuates, it does not diverge. In Fig. 14(b), the peak of $\bar{\theta}_e$ remains within 0.14 rad, and the peak of $\bar{\theta}_e$ in Fig. 14(c) remains within 0.12 rad. When changed to $R_{sa}/R_s = 2$, in both Fig. 14(b) and (c), $\bar{\theta}_e$ suddenly decreases and fluctuates more intensely, but remains stable. Moreover, the peak of $\bar{\theta}_e$ in Fig. 14(b) is still within 0.14 rad, and the peak of $\bar{\theta}_e$ in Fig. 14(c) is still within 0.12 rad. In the sensitivity analysis of L_s, as shown in Fig. 15(a), when the CCSO is employed, $\bar{\theta}_e$ exhibits a divergent trend when $L_{sa}/L_s = 1/2$, with the peak exceeding 0.15 rad. When changed to $L_{sa}/L_s = 2$, $\bar{\theta}_e$ gradually converges back to 0.15 rad. Fig. 15(b) and (c), respectively, present the results obtained by using the adaptive STESO and the adaptive FTDO-based method. It can be seen that whether $L_{sa}/L_s = 1/2$ or $L_{sa}/L_s = 2$, the $\bar{\theta}_e$ in Fig. 15(b) and (c) are not affected. The sensitivity test results of ψ_f are presented in

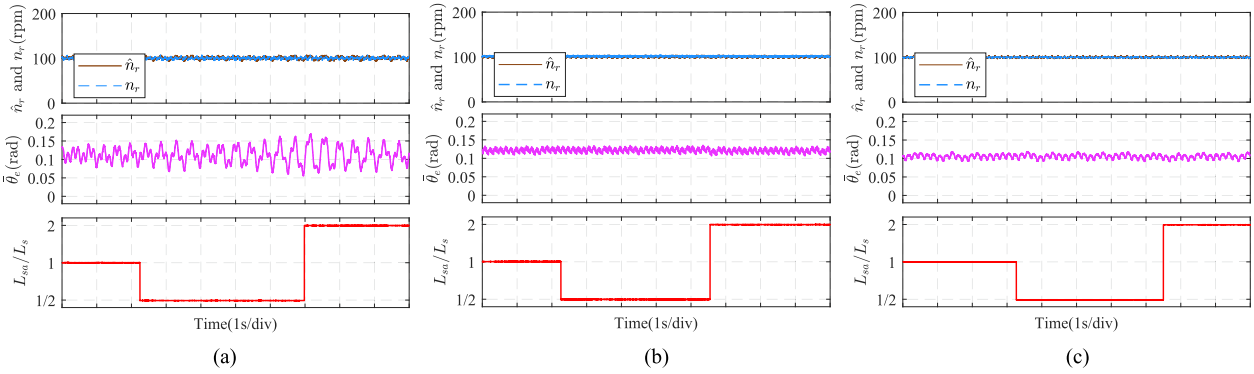

Fig. 15. Experimental results of $\hat{n}_r$, n_r, and $\bar{\theta}_e$ when L_s changes using different observers at 100 rpm. (a) CCSO in [20]. (b) Adaptive STESO in [18]. (c) Proposed adaptive FTDO-based method.

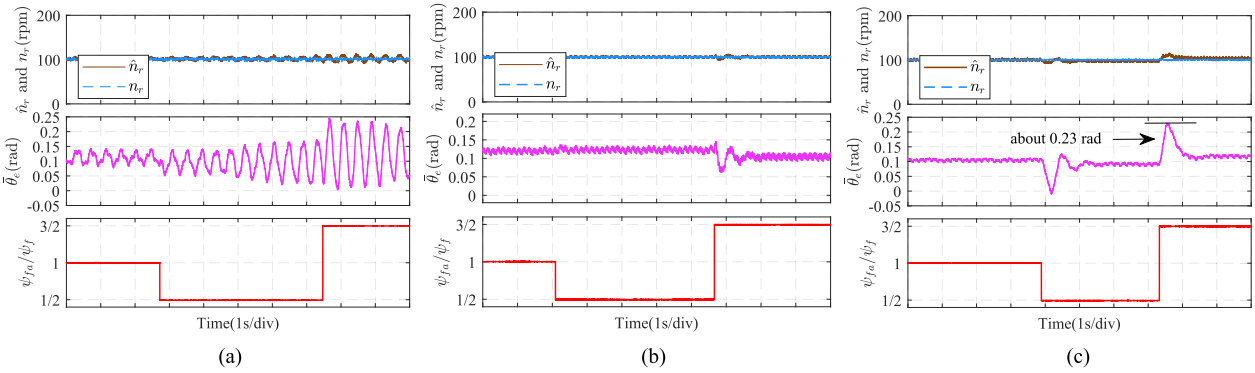

Fig. 16. Experimental results of $\hat{n}_r$, n_r, and $\bar{\theta}_e$ when ψ_f changes using different observers at 100 rpm. (a) CCSO in [20]. (b) Adaptive STESO in [18]. (c) Proposed adaptive FTDO-based method.

Fig. 16. Fig. 16(a) shows the results using the CCSO. After $\psi_{fa}/\psi_f = 1/2$ is set, the fluctuation range of $\bar{\theta}_e$ expands, and the peak exceeds 0.15 rad. When changed to $\psi_{fa}/\psi_f = 3/2$, $\bar{\theta}_e$ increases abruptly, reaching a peak of 0.25 rad, and then slowly converging. In Fig. 16(b), when adopting the adaptive STESO, $\bar{\theta}_e$ only changes and eventually decreases after setting $\psi_{fa}/\psi_f = 3/2$, and the motor still operates stably. In Fig. 16(c), when switched to the adaptive FTDO-based method, with the setting of $\psi_{fa}/\psi_f = 1/2$, $\bar{\theta}_e$ suddenly decreases, and then recovers to around 0.1 rad. After changing to $\psi_{fa}/\psi_f = 3/2$, although $\bar{\theta}_e$ increases to about 0.23 rad, it can converge to within 0.12 rad.

According to the analysis of Figs. 14–16, compared with the CCSO, the proposed adaptive FTDO-based method and the adaptive STESO have significantly lower sensitivity to electrical parameters mismatch, which thanks to the strong robustness of SMC to model parameters.

D. Noise Sensitivity Test

Experimental result of noise robustness using the proposed adaptive FTDO-based method is shown in Fig. 17. In the figure, $\mathrm{V} = U_{\mathrm{inj}} + U_{\mathrm{inj}} \cdot (-1)^{\mathrm{k}}$, which is a high frequency square wave with an amplitude of $2U_{\mathrm{inj}} = 20$ V and a frequency of 5 kHz. The

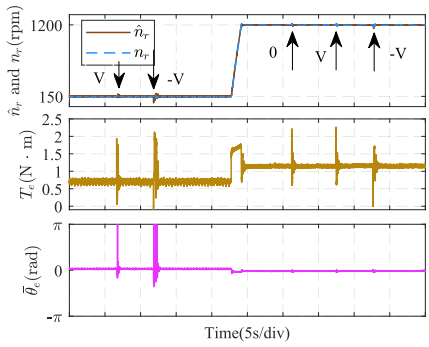

Fig. 17. Experimental result of noise robustness using the proposed adaptive FTDO-based method.

position marked with "V" indicates the start of injecting V into the q-axis stator voltage u_q at this time, the position marked with "$-$V" indicates the start of injecting $-$V into u_q at this time, and the position marked with "0" indicates that no signal is injected. Throughout the entire process, although different high frequency noise signals are injected into u_q, the motor can quickly recover from noise disturbance, indicating the strong robustness of the proposed method to noise. From a theoretical perspective, the strong robustness to noise is attributed to the robustness of

SMC against disturbance and the finite time convergence of the proposed adaptive FTDO.

VI. Conclusion

In this article, to improve the position and speed observation performance of SPMSM, an adaptive FTDO-based position sensorless drive method is proposed. First, by devising an adaptive law and combining it with a fixed time sliding surface, an adaptive FTDO is proposed to observe system disturbance in a finite time. The adaptive law can stably track the bound of the first derivative of disturbance, which has eliminated the need for the bounds of disturbance and its first derivative, and also suppressed the chattering of observed disturbance. Next, an adaptive speed observer is designed by utilizing the proposed adaptive FTDO, which has compensated the disturbance of the estimated flux and realized direct observation of speed. The finite time convergence and stability of adaptive FTDO have been verified by Lyapunov functions. The coefficient setting guides of adaptive FTDO are also given. Finally, the feasibility and effectiveness of the proposed adaptive FTDO-based method are proved by comparative tests on an SPMSM.

Appendix A
Preliminaries

Lemma 1 (See [31]): Suppose there are a positive definite function $V(x) \in C^1$, the initial value of $V(x)$ is V_0, and constants $\ell_1, \mu > 0$, $0 < p_1, \nu_1, \nu_2 < 1$ such that

$$\dot{V}(x) \le -\ell_1 V(x)^{p_1} + \mu \tag{33}$$

holds. In this case, the system will converge in finite time, and the convergence time t_{c1} and the state variable x satisfy

$$t_{c1} \le \frac{V_0^{1-p_1}}{\ell_1\nu_1(1-p_1)}, \quad \{x \in R||x| \le \frac{\mu}{\ell_1(1-\nu_2)}\}. \tag{34}$$

Lemma 2 (See [32]): Assume that a function $V(x) \in C^1$, V_0 is the initial value of $V(x)$, the constants $\ell_2 > 0$ and $0 < p_2 < 1$ exist. If

$$\dot{V}(x) \le -\ell_2 V(x)^{p_2} \tag{35}$$

holds, the equilibrium point $x = 0$ is finite time stable. And the convergence time t_{c2} satisfies

$$t_{c2} \le \frac{V_0^{1-p_2}}{\ell_2(1-p_2)}. \tag{36}$$

Lemma 3 (See [33]): Suppose that a Lyapunov function $V(x)$ in R^n satisfies

$$\dot{V}(x) \le -[r_1 V(x)^m + r_2 V(x)^n]^q \tag{37}$$

where r_1, r_2, m, n, and q are positive constants, besides, the conditions $0 < mq < 1$ and $nq > 1$ need to be satisfied. In this case, the equilibrium point $x = 0$ will converge in fixed time, and the convergence time t_{c3} satisfies

$$t_{c3} \le \frac{1}{r_1^q(1-mq)} + \frac{1}{r_2^q(nq-1)}. \tag{38}$$

Appendix B
Derivative of V_1

Differentiating V_1 yields

$$\begin{aligned}
\dot{V}_1 &= s\dot{s} + \tilde{\eta}\dot{\tilde{\eta}} = s(\Sigma_\gamma + \dot{\gamma} - \dot{d}) - \tilde{\eta}\dot{\hat{\eta}} \\
&= -(\varepsilon + \hat{\eta})|s| - \dot{d}s - \tilde{\eta}(-\chi\hat{\eta} + |s|) \\
&\le (|\dot{d}| - \hat{\eta})|s| - \varepsilon|s| + \chi\tilde{\eta}\hat{\eta} - \tilde{\eta}|s| \\
&\le (\eta - \hat{\eta})|s| - \varepsilon|s| + \chi\tilde{\eta}\hat{\eta} - \tilde{\eta}|s| = -\varepsilon|s| + \chi\tilde{\eta}\hat{\eta} \\
&= -\varepsilon|s| + \chi\tilde{\eta}(\eta - \tilde{\eta}) \le -\varepsilon|s| + \chi(\frac{\eta^2}{2} - \frac{\tilde{\eta}^2}{2}) \\
&= -\varepsilon|s| - \frac{\chi}{2}(\tilde{\eta}^2)^{\frac{1}{2}} + \frac{\chi}{2}(\tilde{\eta}^2)^{\frac{1}{2}} - \frac{\chi}{2}\tilde{\eta}^2 + \frac{\chi}{2}\eta^2 \\
&\le -\min\{\sqrt{2}\varepsilon, \frac{\chi}{\sqrt{2}}\} \cdot (\frac{|s|}{\sqrt{2}} + \frac{(\tilde{\eta}^2)^{\frac{1}{2}}}{\sqrt{2}}) + \delta_1 \\
&\le -\min\{\sqrt{2}\varepsilon, \frac{\chi}{\sqrt{2}}\} V_1^{\frac{1}{2}} + \delta_1
\end{aligned} \tag{39}$$

where $\delta_1 = (\chi + 4\chi\eta^2)/8$.

Appendix C
Derivative of V_2

Differentiating V_2 yields

$$\begin{aligned}
\dot{V}_2 &= s\dot{s} + [f_\gamma(s) - f_\gamma(0)]\dot{f}_\gamma(s) \\
&= -f_\gamma(s)\,|s| - \dot{d}s + 2f_\gamma(s) \cdot [f_\gamma(s) - \varepsilon] \\
&\quad \cdot (-f_\gamma(s) - \dot{d}\mathrm{sign}(s)) \\
&\le -(-\eta + f_\gamma(s))\,|s| - 2f_\gamma(s) \cdot |f_\gamma(s) - \varepsilon| \\
&\quad \cdot (-\eta + f_\gamma(s)) \\
&= -(f_\gamma(s) - \eta) \cdot [|s| + 2f_\gamma(s) \cdot |f_\gamma(s) - \varepsilon|] \\
&= -\sqrt{2}(f_\gamma(s) - \eta) \cdot [\frac{|s|}{\sqrt{2}} + \frac{2f_\gamma(s)\,|f_\gamma(s) - \varepsilon|}{\sqrt{2}}] \\
&\le -\sqrt{2}(f_\gamma(s) - \eta) \cdot \min\{1, 2f_\gamma(s)\}[\frac{|s|}{\sqrt{2}} + \frac{|f_\gamma(s) - \varepsilon|}{\sqrt{2}}] \\
&\le -\sqrt{2}(f_\gamma(s) - \eta) \cdot \min\{1, 2f_\gamma(s)\}V_2^{\frac{1}{2}}.
\end{aligned} \tag{40}$$

If $\varepsilon < \eta$, when s satisfies $s_c < |s| < \delta_0$, since $f_\gamma(s)$ rises monotonically on $[0, \delta_0)$, then $f_\gamma(s) > f_\gamma(s_c) = \eta$ holds, that is, $\dot{V}_2 < 0$ holds. On the contrary, if $\varepsilon \ge \eta$, $|s| > s_c = 0$, then $f_\gamma(s) > f_\gamma(s_c) = \varepsilon > \eta$ holds, and $\dot{V}_2 < 0$ also holds.

References

[1] G. Wang, M. Valla, and J. Solsona, "Position sensorless permanent magnet synchronous machine drives—A review," *IEEE Trans. Ind. Electron.*, vol. 67, no. 7, pp. 5830–5842, Jul. 2020.

[2] J. Chen, X. Yuan, F. Blaabjerg, and C. H. T. Lee, "Overview of fundamental frequency sensorless algorithms for AC motors: A unified perspective," *IEEE J. Emerg. Sel. Top. Power Elect.*, vol. 11, no. 1, pp. 915–931, Feb. 2023.
[3] G. Zhang, S. Li, B. Li, Q. Wang, G. Wang, and D. Xu, "Acoustic noise reduction using half-period-switching pseudorandom sinusoidal injection with external tangent demodulation for sensorless PMSM drives," *IEEE Trans. Transp. Electrific.*, vol. 11, no. 2, pp. 5312–5323, Apr. 2025.
[4] A. Pan et al., "Adaptive Back-EMF observer based on filtered transformation for sensorless SPMSM control," *IEEE Trans. Power Electron.*, vol. 40, no. 11, pp. 16231–16242, Nov. 30, 2025, doi: 10.1109/TPEL.2025.3584399.
[5] J. Liu and Y. Zhang, "Performance improvement of nonlinear flux observer for sensorless control of PMSM," *IEEE Trans. Ind. Electron.*, vol. 70, no. 12, pp. 12014–12023, Dec. 2023.
[6] G. Zhang et al., "Hybrid pseudorandom signal injection for position sensorless SynRM drives with acoustic noise reduction," *IEEE Trans. Transp. Electrific.*, vol. 8, no. 1, pp. 1313–1325, Mar. 2022.
[7] D. Yang et al., "ILADRC-based sensorless IPMSM strategy with adaptive harmonic filtering-extended state observer for current quality improvement," *IEEE Trans. Power Electron.*, early access, Jun., 5, 2025, doi: 10.1109/TPEL.2025.3576892.
[8] D. Jin, L. Liu, Q. Lin, and D. Liang, "Sensorless control strategy of PMSM with disturbance rejection based on adaptive sliding mode control law," *IEEE Trans. Transport. Electrific.*, vol. 10, no. 3, pp. 5424–5438, Sep., 2024.
[9] N. K. Quang, N. T. Hieu, and Q. P. Ha, "FPGA-Based sensorless PMSM speed control using reduced-order extended Kalman filters," *IEEE Trans. Ind. Electron.*, vol. 61, no. 12, pp. 6574–6582, Dec. 2014.
[10] Z. Qiao, T. Shi, Y. Wang, Y. Yan, C. Xia, and X. He, "New sliding-mode observer for position sensorless control of permanent-magnet synchronous motor," *IEEE Trans. Ind. Electron.*, vol. 60, no. 2, pp. 710–719, Feb. 2013.
[11] D. Jin and L. Liu, "Adaptive second-order disturbance observer-based position sensorless drive strategy for PMSM," *IEEE Trans. Power Electron.*, vol. 39, no. 12, pp. 16415–16428, Dec. 2024.
[12] L. Chen et al., "Sensorless fixed-time sliding mode control of PMSM based on barrier function adaptive super-twisting observer," *IEEE Trans. Power Electron.*, vol. 39, no. 3, pp. 3037–3051, Mar. 2024.
[13] I. Boldea, M. C. Paicu, and G.-D. Andreescu, "Active flux concept for motion-sensorless unified AC drives," *IEEE Trans. Power Electron.*, vol. 23, no. 5, pp. 2612–2618, Sep., 2008.
[14] Y. Park and S.-K. Sul, "Sensorless control method for PMSM based on frequency-adaptive disturbance observer," *IEEE J. Emerg. Sel. Top. Power Electr.*, vol. 2, no. 2, pp. 143–151, Jun. 2014.
[15] S. Zhou et al., "A robust encoderless control for PMSM drives: A revised hybrid active flux-based technique," *IEEE Trans. Power Electron.*, vol. 38, no. 11, pp. 14438–14449, Nov. 2023.
[16] D. Jin, L. Liu, and D. Liang, "A flux observer based on a dual-layer adaptive algorithm for SPMSMs position sensorless drive," *IEEE J. Emerg. Sel. Top. Power Elect.*, vol. 13, no. 2, pp. 2358–2371, Apr. 2025.
[17] T. Zhang, Z. Xu, J. Li, H. Zhang, and C. Gerada, "A third-order super-twisting extended state observer for dynamic performance enhancement of sensorless IPMSM drives," *IEEE Trans. Ind. Electron.*, vol. 67, no. 7, pp. 5948–5958, Jul. 2020.
[18] Q. Lin, L. Liu, D. Liang, D. Jin, S. Jia, and H. Song, "A dual-level adaptive law design for super-twisting algorithm in sensorless IPMSM drives," *IEEE Trans. Ind. Appl.*, vol. 59, no. 5, pp. 5945–5956, Sep./Oct. 2023.
[19] K. Shao et al., "Leakage-type adaptive state and disturbance observers for uncertain nonlinear systems," *Nonlinear Dyn.*, vol. 105, pp. 2299–2311, 2021.
[20] S. Ye and X. Yao, "A modified flux sliding-mode observer for the sensorless control of PMSMs with online stator resistance and inductance estimation," *IEEE Trans. Power Electron.*, vol. 35, no. 8, pp. 8652–8662, Aug. 2020.
[21] Y. Liu, H. Li, R. Lu, Z. Zuo, and X. Li, "An overview of finite/fixed-time control and its application in engineering systems," *IEEE/CAA J. Automatica Sinica*, vol. 9, no. 12, pp. 2106–2120, Dec. 2022.
[22] M. Boukattaya, N. Mezghani, and T. Damak, "Adaptive nonsingular fast terminal sliding-mode control for the tracking problem of uncertain dynamical systems," *ISA Trans.*, vol. 77, pp. 4135–4144, May 2018.
[23] J. Ni, L. Liu, M. Chen, and C. Liu, "Fixed-time disturbance observer design for brunovsky systems," *IEEE Trans. Circuits Syst. II, Exp. Briefs*, vol. 65, no. 3, pp. 341–345, Mar. 2018.
[24] J. Sun, J. Yi, Z. Pu, and X. Tan, "Fixed-time sliding mode disturbance observer-based nonsmooth backstepping control for hypersonic vehicles," *IEEE Trans. Syst., Man, Cybern., Syst.*, vol. 50, no. 11, pp. 4377–4386, Nov. 2020.
[25] S. Liu, L. Liu, Q. Lin, and D. Liang, "Fixed-time high-order dynamic observation strategy for PMSM sensorless control," *IEEE Trans. Power Electron.*, vol. 39, no. 12, pp. 16442–16457, Dec. 2024.
[26] Y. Yang, Y. Cui, Y. Zhu, and J. Qiao, "Fixed-time refined disturbance observer-based composite control for periscope-type coarse pointing assembly," *IEEE Trans. Ind. Electron.*, vol. 71, no. 11, pp. 14896–14905, Nov. 2024.
[27] X. Yu, P. Li, and Y. Zhang, "The design of fixed-time observer and finite-time fault-tolerant control for hypersonic gliding vehicles," *IEEE Trans. Ind. Electron.*, vol. 65, no. 5, pp. 4135–4144, May 2018.
[28] M. J. Mirzaei, M. Asadollahi, E. Aslmostafa, and M. A. Badamchizadeh, "Continuous robust control based on fixed-time super-twisting disturbance observer," *IEEE Trans. Syst., Man, Cybern., Syst.*, vol. 54, no. 1, pp. 426–435, Jan. 2024.
[29] H. Wang et al., "Continuous fast nonsingular terminal sliding mode control of automotive electronic throttle systems using finite-time exact observer," *IEEE Trans. Ind. Electron.*, vol. 65, no. 9, pp. 7160–7172, Sep. 2018.
[30] K. Shao, J. Zheng, H. Wang, F. Xu, X. Wang, and B. Liang, "Recursive sliding mode control with adaptive disturbance observer for a linear motor positioner," *Mech. Syst. Signal Process.*, vol. 146, Jan. 2021, Art. no. 107014.
[31] Z. Zhu, Y. Xia, and M. Fu, "Attitude stabilization of rigid spacecraft with finite-time convergence," *Int. J. Robust Nonlinear Control*, vol. 21, no. 6, pp. 686–702, Feb. 2011.
[32] X. Huang, W. Lin, and B. Yang, "Global finite-time stabilization of a class of uncertain nonlinear systems," *Automatica*, vol. 41, no. 5, pp. 881–888, May 2005.
[33] A. Polyakov, "Nonlinear feedback design for fixed-time stabilization of linear control systems," *IEEE Trans. Autom. Control*, vol. 57, no. 8, pp. 2106–2110, Aug. 2012.

Dongsong Jin (Student Member, IEEE) received the B.Sc. degree in electrical engineering from Northeast Electric Power University, Jilin, China, in 2020. He is currently working toward the Ph.D. degree in electrical engineering with the School of Electrical Engineering, Xi'an Jiaotong University, Xi'an, China.

His research interests include sensorless drive of electric machines and disturbance compensation of motor system.

Ling Liu (Senior Member, IEEE) received the B.S. degree in electronic information from Xi'an Polytechnic University, Xi'an, China, in 2003, the M.S.degree in measuring and testing technologies and instruments from Southwest Jiaotong University, Chengdu, China, in 2006, and the Ph.D. degree in electrical engineering from Xi'an Jiaotong University, Xi'an, China, in 2011.

He is currently a Professor with the School of Electrical Engineering, Xi'an Jiaotong University. He has authored or coauthored several technical papers and industrial reports. His research interests include electrical machines, control theory and applications, intelligent diagnosis, and control of electric power equipment.

Dr. Liu is a Senior Member of China Electrotechnical Society.